Large scale turbulent round free jet far field investigations using Shake-The-Box 3D Lagrangian Particle Tracking

T. Buchwald^{1,*}, D. Schanz², P. Godbersen², J. Agocs², A. Schröder^{1,2}

1: Brandenburg University of Technology Cottbus-Senftenberg, Chair of Image Based Measurement Techniques, Cottbus, Germany
2: German Aerospace Center (DLR), Institute of Aerodynamics and Flow Technology, Göttingen, Germany
*Corresponding author: Tom.Buchwald@b-tu.de

Keywords: Free jet, Turbulence, Far field, Lagrangian Particle Tracking, FlowFit

ABSTRACT

In this study, we utilize the Shake-The-Box (STB) Lagrangian Particle Tracking (LPT) algorithm to conduct large-scale measurements in the far field of a turbulent jet. We confirm self-similar mean velocity and Reynold stress profiles across two fields of view (FOVs) spanning 90 to 240 nozzle diameters in streamwise direction. Furthermore, the utilization of a novel version of the data assimilation scheme FlowFit enables the visualization of instantaneous realizations of coherent structures in terms of Q-values. The results indicate that the structures are predominantly tube rather than hairpin-like. The high number of tracked particles and the extensive measurement range allow for the estimation of mean dissipation as a function of the distance from the nozzle using structure functions. A comparison of results derived from longitudinal and transverse approaches with those obtained using the velocity-acceleration structure function indicates that the latter provides more accurate results due to its validity in anisotropic flows. However, the findings also indicate that the anisotropy diminishes downstream. The determination of mean dissipation and acceleration enables the investigation of the validity of the Heisenberg-Yaglom relation in this anisotropic flow. Nevertheless, acceleration is a highly intermittent value, which hinders capturing all relevant events to measure its variance accurately. This paper presents the difficulties encountered in the tracking and filtering of the trajectories, offering a perspective on potential future solutions to the problem.

1. Introduction

Turbulent free jet flows have been a focal point of turbulence research for decades, representing a canonical flow with applications ranging from engineering contexts, such as aircraft engines, combustion, HVAC and heat exchange. Furthermore, it is possible to derive additional general findings from experiments in canonical flows. One example for this is the observation from wake experiments that the initial conditions of free shear flows have a significant impact on the flow far downstream (Bevilaqua and Lykoudis, 1978; Sreenivasan and Narasimha, 1982). These

experiments demonstrated, contrary to widely accepted assumptions at this time, the influence of initial and upstream conditions on the space-time development of turbulence. This behavior is also present in turbulent free jet flows, in which the asymptotic spreading rates have been identified as dependent on initial conditions, a phenomenon extensively discussed in the literature (George, 2012). In other words, turbulence statistics, such as the Reynolds stresses, do not collapse into a profile that is universal for all jet experiments.

The discrepancy between theory and experiment was resolved by the development of the equilibrium self-similarity theory (George, 1989), which takes the influence of the initial conditions into account and thus does not imply equality of the Reynolds stress profiles for different jet experiments. This theory is now widely accepted and proven for the statistical description of jet flows. However, it is important to note that the statistical description only represents a limited aspect of the overall problem. In addition, an analysis of the instantaneous characteristics of the flow reveals coherent structures that establish its evolution (Ball, 2012). It remains unclear how instantaneous realizations of these structures interact with each other and organize under specific initial conditions. Furthermore, little is known about the self-similar scaling and coherent structures in the super-far field (x/d > 150) despite the considerable number of publications on axisymmetric turbulent jets. The reason for that is a lack of data required for such an analysis. Simulation approaches such as Large Eddy Simulation (LES) or Direct Numerical Simulation (DNS) are challenging when examining high Reynolds number flow. The necessity for a large volume coupled with a fine mesh presents significant computational difficulties (Clark and Loth, 2013). However, investigating the far field of a jet experimentally is also challenging because measurements far downstream are highly sensitive to the influence of confining walls. As discussed by Hussein et al. (1994), the return flow interacts with the jet, distorting both the spreading rate and the half width of the jet. Furthermore, conventional experimental methods, such as Hot-Wire Anemometry (HWA), are unable to provide spatially high resolved measurements. Therefore, this study employs Shake-The-Box (STB) Lagrangian Particle Tracking methodology (LPT) (Schanz et al., 2016; Schröder and Schanz, 2023) in a 1.85 m volume embedded in an 82 m³ large test room and the data assimilation technique FlowFit (Gesemann et al., 2016; Godbersen et al. 2024). These methods enable time-resolved capturing of velocity, acceleration, and their respective gradients across the entire 3D flow field, allowing for a comprehensive examination of the turbulent free jet flow. Particularly interesting in this context is the acceleration variance and turbulent kinetic energy dissipation, because the Heisenberg-Yaglom relation (Monin and Yaglom, 1975)

$$\langle a_i a_j \rangle = a_0 \varepsilon^{\frac{2}{3}} v^{-\frac{1}{2}} \delta_{ij}$$

connects both values using a dimensionless variable a_0 , which they proposed to be a constant for sufficiently large Taylor length scale-based Reynolds numbers Re_λ . It has been shown through DNS (Yeung et al., 2006) and experiments (Lawson et al. 2018; Voth et al., 2002) that a_0 does not level off for $Re_\lambda < 500$. Previous efforts to measure a_0 were focused on homogeneous isotropic turbulence. One exception is the study of a turbulent free jet by Viggiano et al. (2021) who investigated the downstream component of acceleration variance in an LPT experiment. In such experiments, tracer particles with a normalized particle diameter d_p/η of less than 5 are required to accurately capture acceleration (Voth et al., 2002). However, their measurements did not meet this criterion, preventing them from drawing definitive conclusions on the influence of anisotropy on a_0 . As the experiment presented here was conducted much further downstream, a smaller normalized particle diameter is reached enabling investigation of acceleration variance without the influence of finite particle size effects.

The article is structured as follows. Section 2 provides a description of the experimental procedure and data processing. Section 3 addresses the question of whether the self-similarity of mean velocity profiles and Reynolds stresses extends also in the super far field. This is followed in section 4 by a discussion of the influence of the jet enclosure. A visualization of coherent structures and their spatial and temporal evolution is presented in section 5. Section 6 discusses the possibilities for estimating dissipation using structure functions, followed by an evaluation of the Heisenberg-Yaglom relation to determine the acceleration variable a_0 in section 7.

2. Experiment and procedure

This paper presents an experimental investigation of the flow in the far field of a round turbulent jet at distances from the nozzle of 90 < x/d < 170 and 160 < x/d < 240, respectively. The experiments were conducted in a large test room measuring 6 4 3.4 m^3 = 82 m^3 , with blackened walls on three sides and a tent-like ceiling (crest height at ~4 m along 6 m) made of black cloth as shown in Figure 1a. Air was expelled horizontally at a velocity of $U_j = 49.75 \text{ m/s}$ and a height of ~1.25 m above the floor at the measurement position using a circular contraction nozzle (see Figure 2) with a diameter of d = 10 mm, resulting in a Reynolds number of $Re_d = 33,000$. Prior to recording, the room was filled with submillimeter sized ($d_p = 350 \text{ µm}$) Helium Filled Soap Bubbles (HFSBs). The HFSBs were illuminated by a large array of LEDs on the floor ($1.6 \text{ } 1.6 \text{ } \text{m}^2$ with a round aperture of 1.25 m diameter) and a smaller one on the ceiling. To increase the reconstructable particle concentration, a scanning approach was applied, where the two halves of the LED array were operated alternately (see Schanz et al. 2024). The camera system consisted of four Vision

Research Phantom v2640 and one v1840 cameras, which recorded 2 · 6294 consecutive images per run. The LEDs and cameras were synchronised at a frequency of 2 · 2 kHz for the first field of view (FOV) and 2 · 1 kHz for the second one. The cameras were located outside the room behind a polycarbonate glass wall. Figure 1b illustrates the positioning and field of view (FOV) of each camera. The three innermost cameras were equipped with f = 50 mm Zeiss Planar lenses, while the outermost cameras were fitted with f = 60 mm Zeiss Macro Planar lenses. The particle images were processed using the Variable-Timestep-Shake-The-Box (VT-STB) LPT method, as described by (Schanz et al., 2021). This method, combined with the scanning approach, allowed for an effective seeding density of over 0.1 particles per pixel. Approximately 400,000 HFSBs were simultaneously tracked within each measurement run and for the two considered regions. In a second step, these are used as input for the linear version of FlowFit3 (Godbersen et al. 2024) to obtain continuous fields of velocity and acceleration. The basic idea of FlowFit is to optimise a set of weights for B-spline basis functions using the velocity and acceleration data along the tracked tracer particles so that the result conforms to the Navier-Stokes equations and mass continuity. The main difference of FlowFit3 compared to its predecessor, FlowFit2 (Gesemann et al., 2016), is that the optimization is operating with a projection onto divergence-free basis functions, so deviations from mass continuity do not have to be further specified as a penalization target. The fields can be reconstructed more accurately and efficiently using this method. A detailed account of the procedure can be found in Godbersen et al. (2024). The continous fields provide velocity gradients which are the basis for the computation of Q-values to visualize vortical structures.

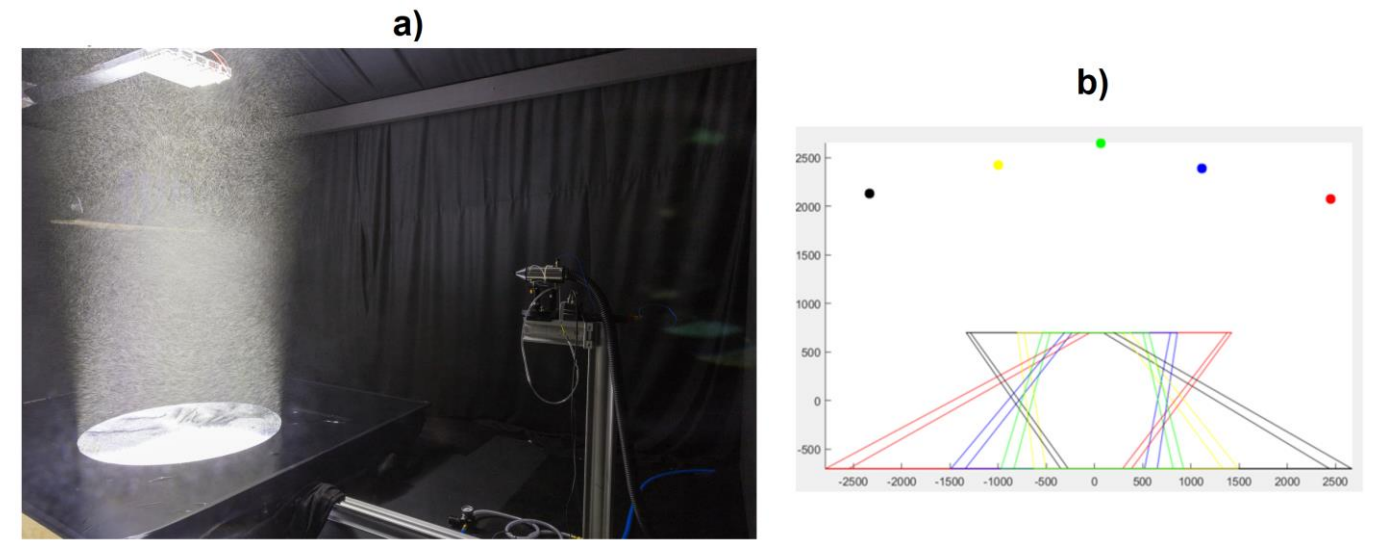


Figure 1: Experimental setup. (a) 82 m 3 test room with LED arrays illuminating the cylindrical STB measurement volume and a d=10mm nozzle. (b) top view of calibrated camera system, showing the common illuminated volume of ~1.85 m 3

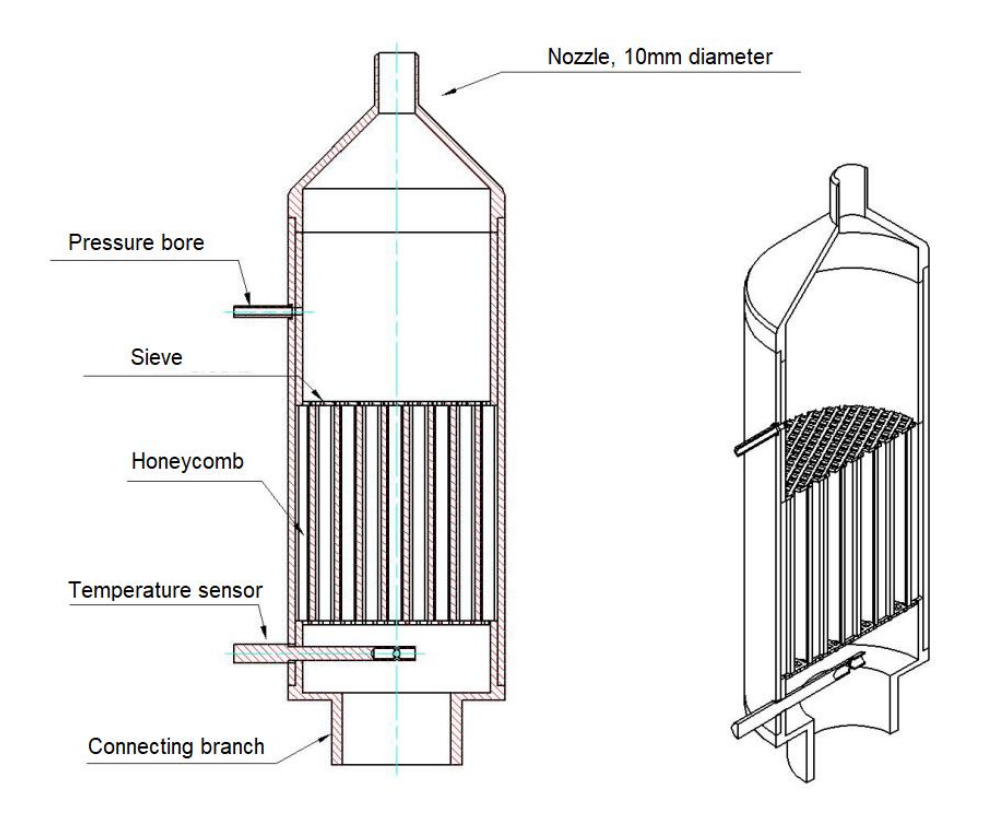


Figure 2: Sketch of the contraction nozzle.

3. Jet characteristics and self-similarity

The velocity distribution and shape of the jet were measured without any symmetry assumptions by carrying out a 3D track binning in the entire measurement volume with a bin size of 15x15x15 mm³. Mean velocity profiles from various source conditions collapse when scaled with appropriate length and velocity parameters in the far field of axisymmetric turbulent jets. Determining these parameters enables the prediction of statistical properties of the jet's future evolution. A common option for this purpose is a scaling by the centerline velocity $U_0(x)$ and the half radius $r_{1/2}(x)$. However, to collapse Reynolds stress profiles, it is also necessary to consider the curvature of the half-width, which leads to a scaling with $U_0(x) dr_{1/2}(x)/dx$. Previous experiments have shown that $r_{1/2}(x)$ is linear, which allows the definition of a constant spreading rate $S = dr_{1/2}(x)/dx$.

Figure 3 displays the scaled mean and variance of streamwise velocity. The profiles of mean velocity are self-similar, even in the super far field. The variance also exhibits self-similarity, although this is less pronounced in the jet center. The reason for this phenomenon may be attributed to the jet exhibiting slight meandering behavior, which is potentially attributable to the

backflow occurring through the boundary of the measuring chamber. This issue is elucidated in greater detail in the subsequent section. In order to accommodate this anomaly, the maximum velocity was adjusted to the center of the cross-section for each position on the x-axis. The observation that, despite this adjustment, the velocity variance profiles does not collapse perfectly, suggests that second order moments of velocity have become decoupled from the mean velocity profile as a consequence of the backflow.

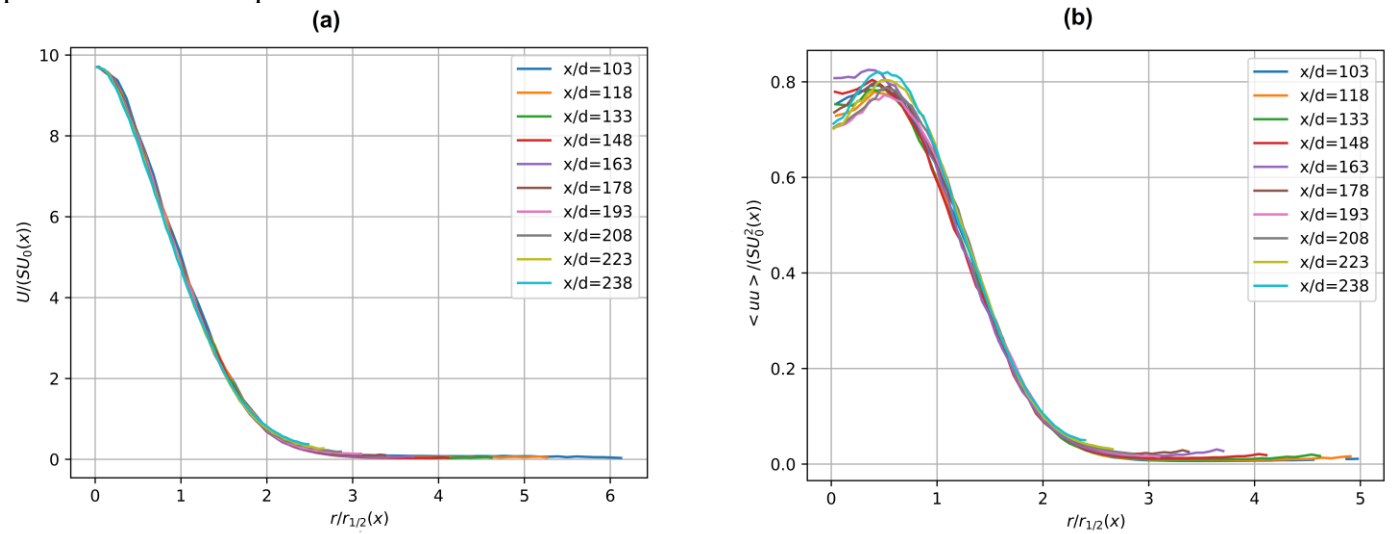


Figure 3: Radially averaged binning results. (a) Average streamwise velocity profiles. (b) Streamwise velocity variance profiles.

Another well documented observation in turbulent jet flows is an inversely proportional relation between the velocity along the centerline and the axial position. The relationship is typically presented in the form

$$\frac{U_0(x)}{U_i} = \frac{B}{(x - x_0)/d}$$

with B denoting the velocity decay rate and x_0 the virtual origin. Figure 4a displays the mean streamwise velocity on the plane z = 0, while the velocity centerline is represented as a grey line. Figure 4b illustrates the results from the individual bins on the centerline, confirming an inverse proportionality.

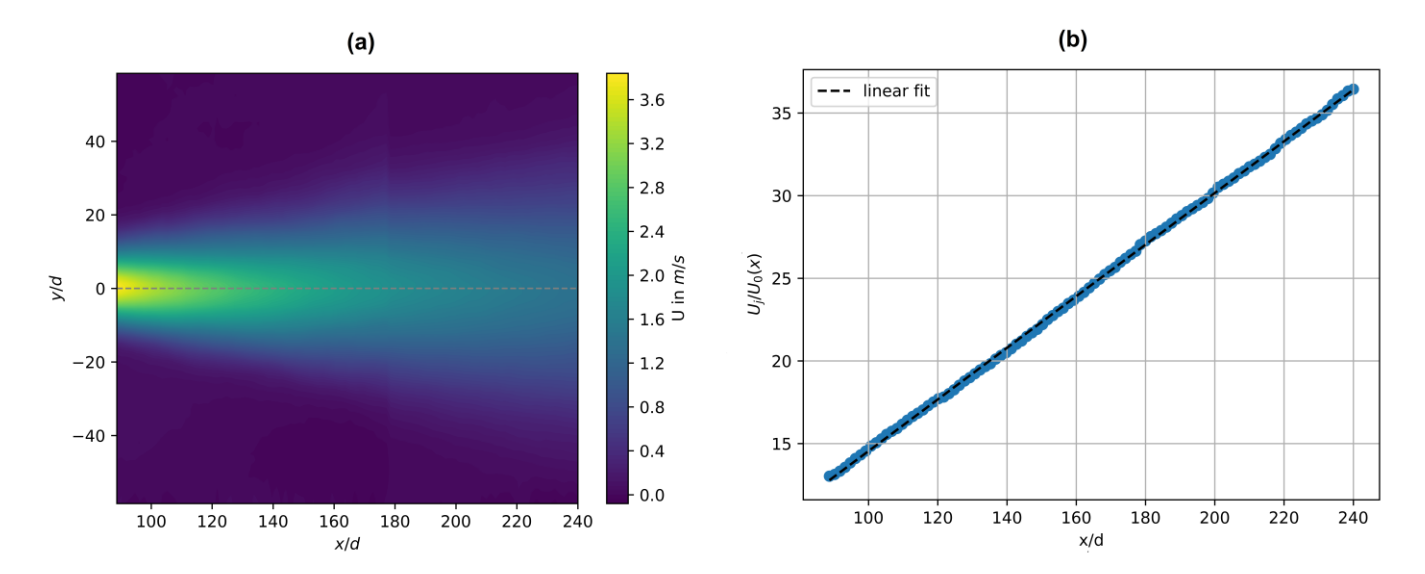


Figure 4: Binning results. (a) Mean streamwise velocity at z=0. (b) Velocity decay represented by each bin on the velocity centerline (blue dots) and their respective linear fit (black line).

It is important to note that the exit velocity is calculated from the pressure behind the nozzle, and therefore has limited accuracy. In order to combine both FOVs, the x-coordinate of the first FOV was adjusted by 7.22cm, ensuring that the velocity on the centreline in the overlap area matched. This is possible because the drop in velocity is linear, such that a shift in the x-axis corresponds to a change in the exit velocity.

A comparison of the present results to the literature is provided in Table 1. While the spreading rate S is consistent with previous findings, the velocity decay rate B is slightly elevated. This phenomenon may be attributed to the effects of confining walls.

	Panchapakesan and	Hussein et al.,	Hussein et al,	Kuhn et al.,	Kwon and	This
	Lumley, 1993	1994	1994	2018	Seo, 2005	contribution
Method	Shuttle-mounted HWA	Flying HWA	LDA	Stereo PIV	PIV	STB-LPT
Domain	30 <x d<160<="" td=""><td>16<x d<124<="" td=""><td>76<x d<100<="" td=""><td>35<x d<95<="" td=""><td>15<x d<75<="" td=""><td>90<x d<240<="" td=""></x></td></x></td></x></td></x></td></x></td></x>	16 <x d<124<="" td=""><td>76<x d<100<="" td=""><td>35<x d<95<="" td=""><td>15<x d<75<="" td=""><td>90<x d<240<="" td=""></x></td></x></td></x></td></x></td></x>	76 <x d<100<="" td=""><td>35<x d<95<="" td=""><td>15<x d<75<="" td=""><td>90<x d<240<="" td=""></x></td></x></td></x></td></x>	35 <x d<95<="" td=""><td>15<x d<75<="" td=""><td>90<x d<240<="" td=""></x></td></x></td></x>	15 <x d<75<="" td=""><td>90<x d<240<="" td=""></x></td></x>	90 <x d<240<="" td=""></x>
Re	11,000	95,500	95,500	17,000	5142	33,000
S	0.096	0.102	0.094	0.091	0.106	0.103
В	6.06	5.9	5.8	6.1	5.5	6.4

Table 1: Comparison of spreading rate S and velocity decay rate B of free round jet experiments, conducted with different measurement techniques.

Figure 5 presents a visualisation of one of the axial velocity variance components. As expected, the self-similarity observed in this case also holds in the super far field.

A visualization of the mean radial acceleration component A_2 and $a_{RMS} = \sqrt{(\langle a_1 a_1 \rangle + \langle a_2 a_2 \rangle + \langle a_3 a_3 \rangle)/3}$ is presented in Figure 6. The mean radial acceleration exhibits its streamwise maxima and minima along the mixing layer. Ring-like vortices form along these layers in the near field (Alekseenko et al., 2018), which exhibit a pressure minimum and thus suck in air from the outside. The present results suggest that the pressure minima persist well into the far field. However, the low values of A_2 in comparison to a_{RMS} indicate that this effect is small.

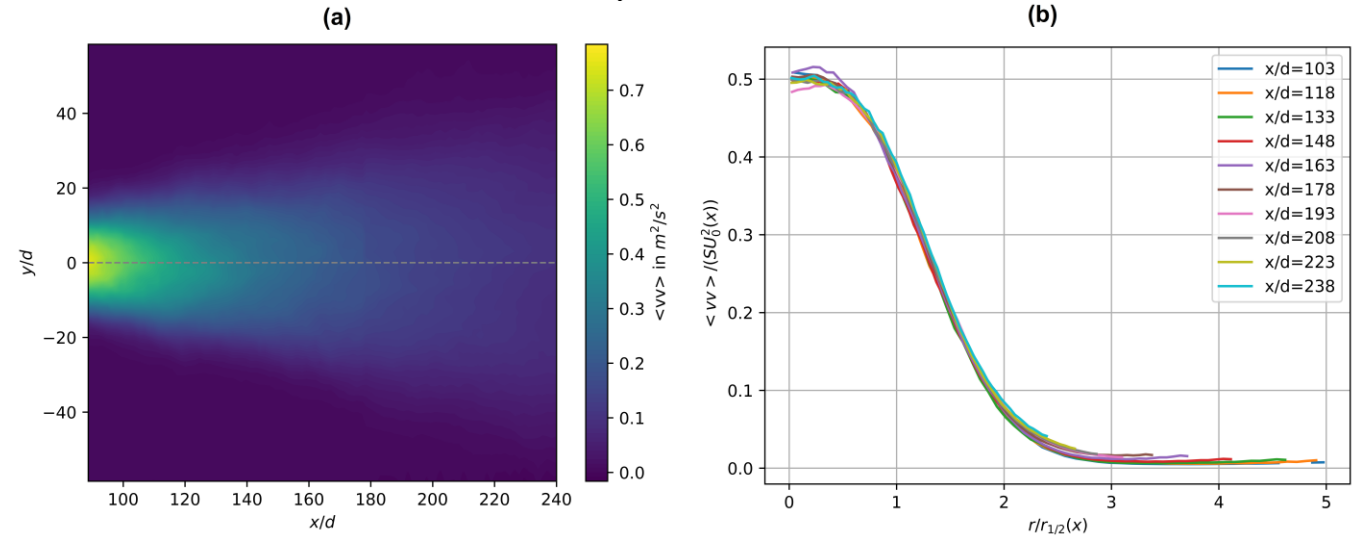


Figure 5: Binning results. (a) Radial velocity variance at z=0. (b) Radially averaged radial velocity variance profiles.

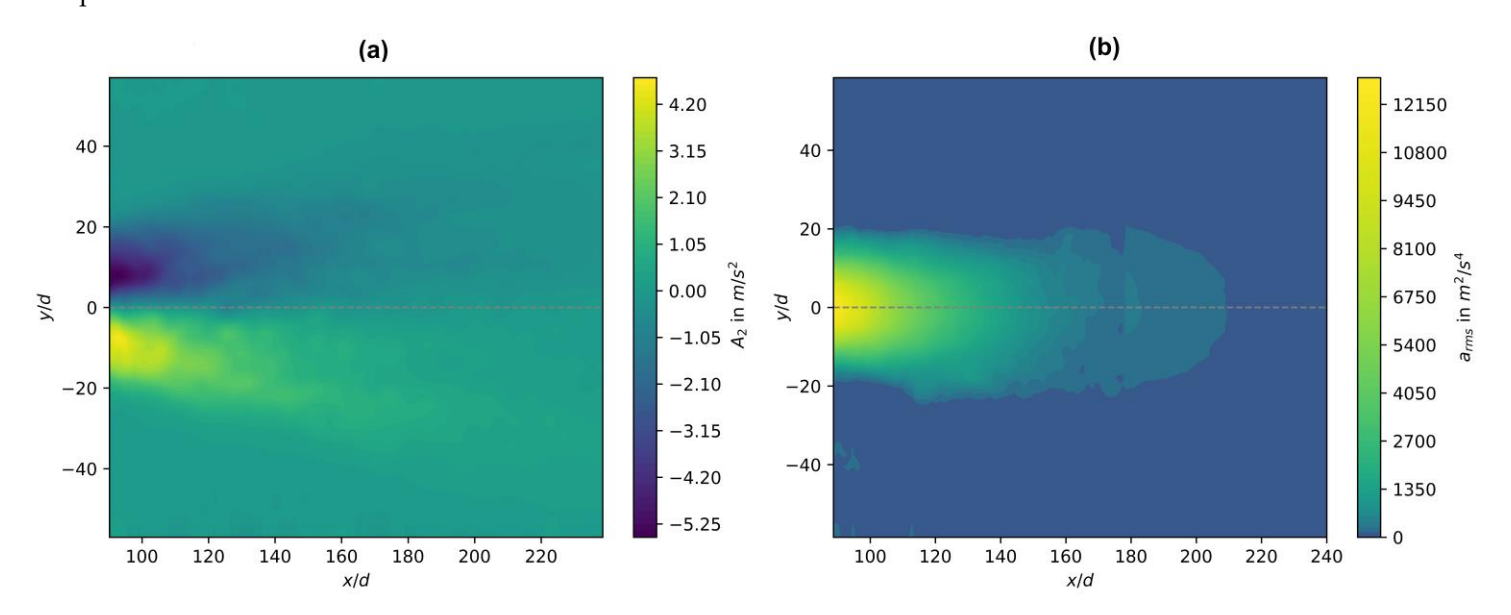


Figure 6: Binning results at z=0. (a) Radial acceleration. (smoothed for clarity) (b) Root mean square of acceleration variances.

4. The effect of confinement on the jet

An experimental study of free jets is essentially a measurement of a confined jet, assuming that the confinement does not significantly modify the flow field. Hussein et al. (1994) argue that earlier measurements, such as those by Capp (1983) and Wygnanski and Fiedler (1969), which showed an increase in velocity decay rate downstream, violated this implicit assumption.

Their argument is based on the fact that momentum conservation requires the momentum integral at each cross section of the measurement facility to be equal to the rate of momentum provided at the source. They propose a model for the effect of confinement on momentum conservation, which allows for an assessment of whether the jet behaves like a free jet or a confined one, significantly altered by backflow.

As the backflow is fed by the momentum from the source, this results in a loss of momentum in the jet. To estimate the influence of this effect, the equality

$$\frac{M}{M_0} = \left[1 + \frac{16}{4B^2} \left(\frac{x}{d}\right)^2 \frac{A_0}{A_R}\right]^{-1}$$

is proposed, in which M represents the momentum of the jet-like parts of the flow field, M_0 represents the total momentum, and A_0 and A_r represent the cross-sectional area of the nozzle outlet and the cross-sectional area of the measurement facility, respectively. For the experimental facility described in this paper, the values of A_0 and A_r are $7.85 \cdot 10^{-5}$ m² and 13.6 m², respectively. This results in $\frac{M}{M_0} = 0.97$ for downstream location $\frac{x}{d} = 240$, which means that the momentum of the jet-like parts contributes more than 97% to the total momentum in the whole measurement area. Thus, the departure from self-similarity of streamwise velocity variance cannot be explained with a loss of momentum due to the backflow.

However, the influence of turbulence or mean pressure differences is not considered in the discussed momentum conservation criterion. This means that it provides only a necessary criterion for estimating whether the jet can be described as free, but it is not sufficient on its own. In fact, the asymmetry of radial velocity variance profiles shown in Figure 4b and the elevated velocity decay rate B hints an additional departure from ideal free jet conditions. The reason for this could be an asymmetry in the pressure field induced by the shape of the jet enclosure caused by placing the LED arrays on the floor and ceiling as shown in Figure 1a.

Coherent structures

It is known for decades that coherent structures are present and persist over time in the self-similar region of turbulent jets (Yoda et al, 1992). As stated by Tso and Hussain (1988), helical structures represent the most prevalent vortical coherent structures and exhibit a pronounced radial outward movement, which in turn enhances the induced speed of the ambient fluid. They conclude that the helical structures may be a significant mechanism for momentum transfer and jet spreading. Later Stereo PIV experiments found hairpin-like structures instead of helical ones (Matsuda and Sakakibara, 2005). However, a comprehensive description of shape, amplitude and evolution of these structures without relying on Taylors frozen turbulence hypothesis require three-dimensional measurement capabilities. The development of Tomo-PIV permitted the execution of such experiments, which demonstrated a high degree of agreement with the picture of hairpin vortices. (Staack et al. 2010, Casey et al., 2013).

The results demonstrated the appearance of hairpin-like structures in the $2 < \frac{x}{d} < 15$ and $30 < \frac{x}{d} < 70$ regions, which are subsequently ejected into the irrotational region. The head of these structures undergoes a reduction in size during downstream advection, ultimately leading to the formation of two vortex tubes. However, the instantaneous velocity fields and Q-value iso-contour-surfaces discussed in this contribution, as shown in Figure 7, rarely exhibit hairpin-like structures. Instead, tube-like structures are apparent, as observed also in homogeneous isotropic turbulence (HIT). The greater distance from the nozzle in the dataset presented here, indicates that the hairpin structures are not produced in the far field and are already disintegrated on their way downstream. It is noteworthy that backflow can be observed at the turbulent/non-turbulent interface of the jet. The Q-value iso-contour-surfaces reveal that larger vortex tubes, which are typical in turbulent flows, are significant carriers for radial momentum exchange. Additionally, the vortex tubes do not significantly decrease in size downstream within the investigated domain, suggesting their long-term durability. On the other hand, they decay over time when advected downstream in terms of absolute Q-values as indicated by the three various thresholds of iso-surface contours presented in Figure 7 b)-d) for the same time-step.

The small-scale turbulence properties are often quantified by means of energy dissipation ε and enstrophy $v\omega^2$, with ω denoting vorticity. Figure 8 shows iso-contour surfaces of both properties simultaneously, allowing for the visualization of their relationship. It can be observed that high enstrophy occupies slightly more space than high dissipation. Additionally, high enstrophy tends to exhibit a tube-like shape, whereas high dissipation manifests as sheet-like structures between those tubes. This is consistent with previous findings (Ganapathisubramani et al., 2008).

Furthermore, our results indicate that high enstrophy events occasionally coexists with high dissipation, although rarely occurring at the same location. This is consistent with the results of DNS in HIT for moderate Reynolds number($Re_{\lambda} > 400$) reported by Yeung et al. (2015).

The results indicate that, at a considerable distance downstream, the coherent motions exhibit similarities to those observed in HIT. However, it is important to note that the interparticle distance is too large to allow definitive conclusions based on the FlowFit3 results. A comprehensive analysis of coherent structures and statistical properties of the velocity gradients is only possible once the problem of smoothing imposed by currently used data assimilation schemes has been solved. Methods based on machine learning (Zhou et al., 2024) have already demonstrated promising results for particle tracking data with high inter-particle distance, and therefore have the potential to enable such investigations using this dataset in future.

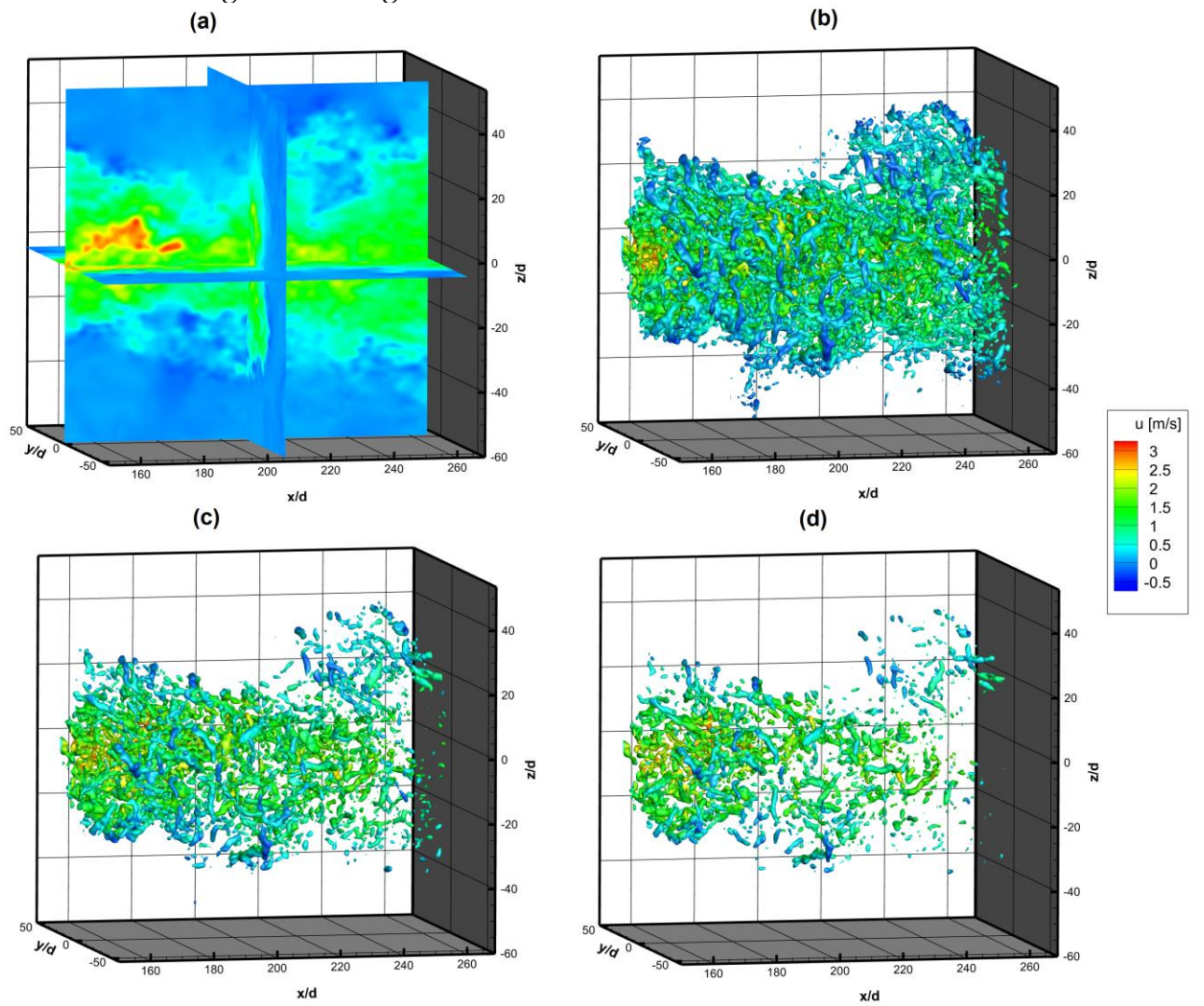


Figure 7: FlowFit3 result showing an instantaneous flow field. (a) Streamwise velocity distribution. (b, c, d) Isosurfaces of Q-values color coded by streamwise velocity with a threshold of 1000 s^{-2} , 1500 s^{-2} and 2000 s^{-2}

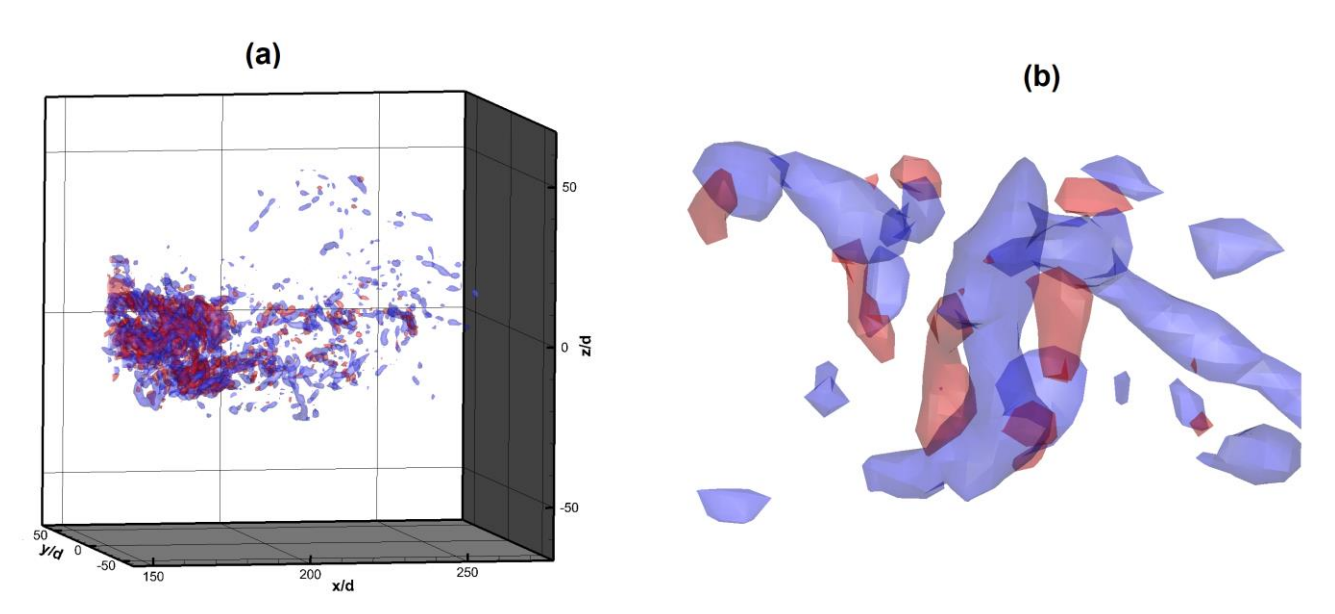


Figure 8: FlowFit3 result showing instantaneous isosurfaces (a) with a threshold of $0.1 \text{ m}^3/\text{s}^2$ of dissipation (red) and enstrophy (blue) in a full measurement volume and (b) of a zoomed in example structure with a threshold of $0.25 \text{ m}^3/\text{s}^2$.

6. Dissipation estimation

The FlowFit3 data assimilation method can be used to calculate local dissipation and enstrophy by generating continuous velocity fields and their derivatives from the particle tracks using third-order divergence-free B-splines. This enables the direct determination of local dissipation from the rate-of-strain tensor S_{ij} by $\varepsilon = 2vS_{ij}S_{ij}$ and enstrophy $v\omega^2$ from the vorticity vector.

However, the local gradients are systematically underestimated if the inter-particle distance is too high (Sciacchitano et al., 2021). Tests with the predecessor FlowFit2 in a von Kárman flow have shown that the mean dissipation is underestimated by more than 30% at a mean inter-particle distance of about 6η (Schröder et al., 2022). Since the mean inter-particle distance is even higher in this large-scale experiment, it is necessary to determine the dissipation with other methods.

Alternatively, in the inertial regime structure functions can be used for this purpose, calculated for partial volumes along the centerline at various downstream positions. However, the well-known velocity structure functions based solely on longitudinal or transversal velocity differences are predicated upon the assumptions of homogeneity and isotropy.

Therefore, this section compares various methods of utilizing structure functions to estimate the

impact of anisotropy and inhomogeneity. One approach, as demonstrated by Viggiano et al. (2021), involves utilizing the transversal structure function

$$S_{2D}(x, r) = \langle [u_1(xe_1 + r) - u_1(xe_1)]^2 \rangle = \frac{4}{3}C_2(\langle \varepsilon(x) \rangle_S |r|)^{\frac{2}{3}}$$

considering separations $\mathbf{r} = (0 \ y \mathbf{e_2} \ z \mathbf{e_3})^T$ forming planes perpendicular to the jet centerline, to compute the centerline dissipation $\langle \varepsilon(x) \rangle_S$ of slices S with an edge length of $l_S < r_{1/2}/3$ and a thickness of less than two particle diameters. According to Pope (2000), the universal constant C_2 is chosen to be 2.

The advantage of this approach is that it enables a high resolution of the average value of $\langle \varepsilon(x) \rangle_S$ on the x-axis by restricting to a quasi-two-dimensional plane. However, it only takes the streamwise velocity fluctuation u_1 into consideration. Romano and Antonia (2000) demonstrated that the large-scale anisotropy observed in turbulent jets, as identified by the ratio between axial and radial velocity fluctuations σ_u/σ_v being greater than 1, results in deviations from K41 theory when calculating structure function exponents. This implies that the anisotropy of free jet flows can only be accurately quantified when both axial and radial separations are considered.

Therefore, the estimates presented below are based on the evaluation of separations r in all three spatial directions. Consequently, the volumes considered in the following are cubes C with an edge length $l_C < r_{1/2}/3$. With the longitudinal velocity increments

$$\delta u_l(x, r) = (u(xe_1 + r) - u(xe_1)) \frac{r}{|r|}$$

K41 theory yields

$$S_{2,l}(x, \mathbf{r}) = \langle \delta u_l(x, \mathbf{r})^2 \rangle = C_2(\langle \varepsilon(x) \rangle_C |\mathbf{r}|)^{\frac{2}{3}}$$

for the longitudinal structure function, while

$$S_{2,t}(x,r) = \langle 0.5[|u(xe_1+r) - u(xe_1)|^2 - \delta u_l(x,r)^2] \rangle = \frac{4}{3}C_2(\langle \varepsilon(x) \rangle_c |r|)^{\frac{2}{3}}$$

applies for the transversal counterpart. Additionally, the velocity-acceleration structure function

$$\langle [u(xe_1+r)-u(xe_1)][a(xe_1+r)-a(xe_1)]\rangle = -2\langle \varepsilon(x)\rangle_{\mathcal{C}}$$

is utilized, which does not assume isotropy. (Mann et al., 1999)

Figure 9 shows structure functions to estimate $\langle \varepsilon(x) \rangle_S$ and $\langle \varepsilon(x) \rangle_C$ at four positions on the centerline.

The structure function of velocity-acceleration displays a plateau for all downstream positions. However, the data has not yet fully converged, despite averaging radially. The methods based on $S_{2,l}(x, \mathbf{r})$ and $S_{2,t}(x, \mathbf{r})$ converge more quickly, but deviate from the expected 2/3 scaling, making it impossible to identify a plateau over a wide range of scales. The extent to which a departure from 2/3 scaling is observed decreases with downstream distance to the nozzle, indicating a reestablishment to locally isotropic conditions far downstream. In order to obtain accurate values

for the dissipation also upstream, the acceleration-velocity structure function is employed for the estimation.

The three methods based on separations in all directions indicate comparable values for dissipation when only short separations are considered. Conversely, the estimate based on $S_{2D}(x, r)$ indicates elevated values for all downstream positions. An explanation consistent with the findings of Romano and Antonia (2000) could be that only the axial position is considered, which fluctuates more strongly than the radial ones. Therefore, the methods based on separations with components in all three dimensions are expected to provide a more accurate estimate. Figure 10 illustrates the dissipation ε obtained from the plateaus of the velocityacceleration structure function considering separations between 2cm and 6cm as well as the transversal Taylor microscale, computed assuming HIT conditions according to $\lambda = \sqrt{15\nu\sigma_u^2/\epsilon}$. The consistency of the evolution of and λ from both overlapping FOVs provides evidence of the validity of the results and leads to an estimation of $Re_{\lambda} = \sigma_u \frac{\lambda}{v} \approx 260$. A direct determination of λ via the curvature of the velocity autocorrelation, without the assumption of isotropy, promises a more accurate estimation. However, this requires a binning with high resolution. It is assumed that this can be achieved with the dataset presented here, provided that intermediate particle positions (lying temporally between the recording times) are also used for binning in order to achieve convergence of the autocorrelation. This approach also permits the determination of the local error introduced by the conventional HIT λ -estimation method.

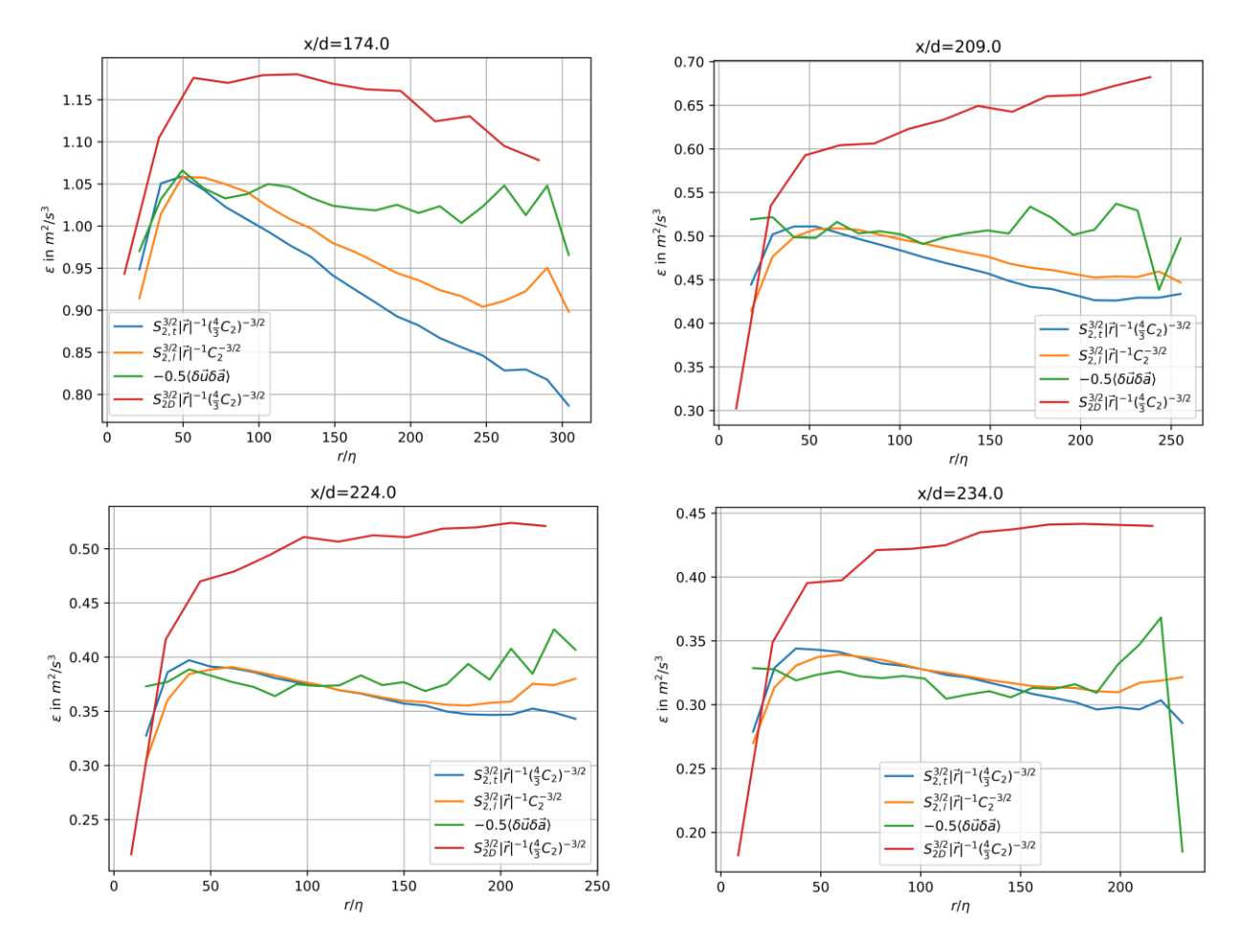


Figure 9: Estimation of mean dissipation on the centerline over absolute particle separation at four downstream distances.

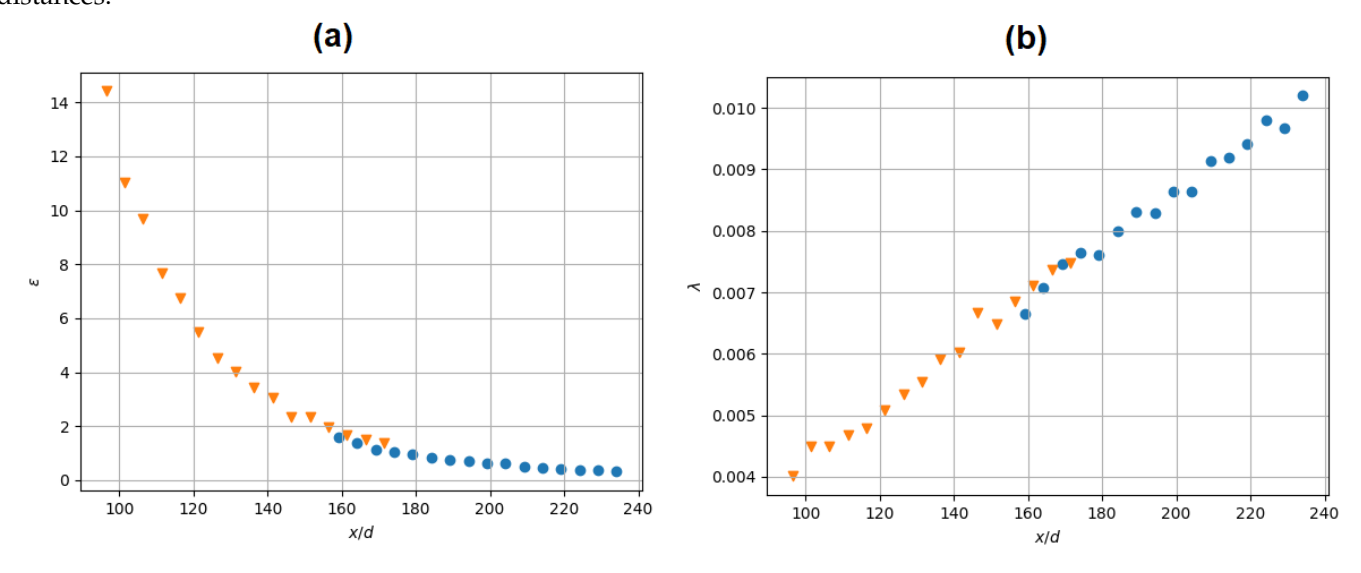


Figure 10: Results inferred from acceleration-velocity structure functions based on first (yellow triangles) and second (blues dots) FOV. (a) Turbulent kinetic energy dissipation and (b) Taylor microscale on the centerline in meters.

7. Acceleration variance scaling

The dataset is suitable not only for investigating jet specifics but also for general turbulence theory. One example for this is the relationship between acceleration variance and dissipation, which is of great importance for some turbulent mixing, dispersion and combustion models (La Porta et al., 2001). Monin and Yaglom (1975) proposed the prediction that

$$\langle a_i a_j \rangle = a_0 \varepsilon^{\frac{2}{3}} v^{-\frac{1}{2}} \delta_{ij}$$

based on Kolmogorov's self-similarity hypothesis, where a_0 is a universal constant given sufficiently high Reynolds number. Voth et al. (2002) conducted an experimental test of the Heisenberg-Yaglom prediction at the highest Reynolds number to date. They measured a_0 using a silicon strip detector, commonly used in particle physics experiments, in a von Kármán flow. This enabled measurements with a maximum Re_{λ} of nearly 1000. The results indicate that a_0 converges for $Re_{\lambda} > 500$. However, precise determination of dissipation was not possible due to the limitations of the strip detector, which only allows for single-point measurements.

Alternative models predict that a_0 does not converge for high Reynolds. An example of this is the model proposed by Borgas et al. (1993), which is based on an extension of the concept of multifractality to Lagrangian acceleration. The model yields

$$a_0(Re_{\lambda}) = \frac{1.9Re_{\lambda}^{0.135}}{1 + \frac{85}{Re_{\lambda}^{0.135}}}$$

which agrees with DNS as well as experiment data in the region $Re_{\lambda} < 680$. (Sawford et al., 2003; Lawson et al. 2018). However, a DNS with higher Reynolds number was recently presented, challenging the reported acceleration constant predicted by Borgas model for $Re_{\lambda} > 1000$. (Buaria and Sreenivasan, 2022). The authors argue that the acceleration intermittency cannot be described by the Eulerian dissipation rate intermittency as it was conjectured by Borgas, because acceleration intermittency is significantly stronger than its Eulerian dissipation counterpart. However, the $Re_{\lambda} \approx 260$ in the current experiment is located in a transition region of the low reynolds number limit with $a_0 \sim Re_{\lambda}$ (Batchelor, 1953) and the high reynolds number region (Sawford et al., 2003), such that the prediction from Borgas model is sufficient. The prediction for $Re_{\lambda} = 260$ is $a_0 = 3.5$, which is in agreement with experiments and simulations conducted in HIT. However, the model's ability to predict flows with stronger anisotropies remains unclear.

In order to answer this question, the tracer particles must accurately capture the acceleration variance, which require a normalized particle diameter of $d_p/\eta < 5$, as previous studies have

shown (Qureshi et al., 2007; Volk et al., 2011). The present experiment meets this requirement over the full range of investigated distances from the nozzle. Figure 11a shows a_0 in relation to the downstream position, demonstrating a deviation from the expected $a_0 = 3.5$. On the contrary, a linear scaling with downstream distance for the data obtained in the second FOV is observed.

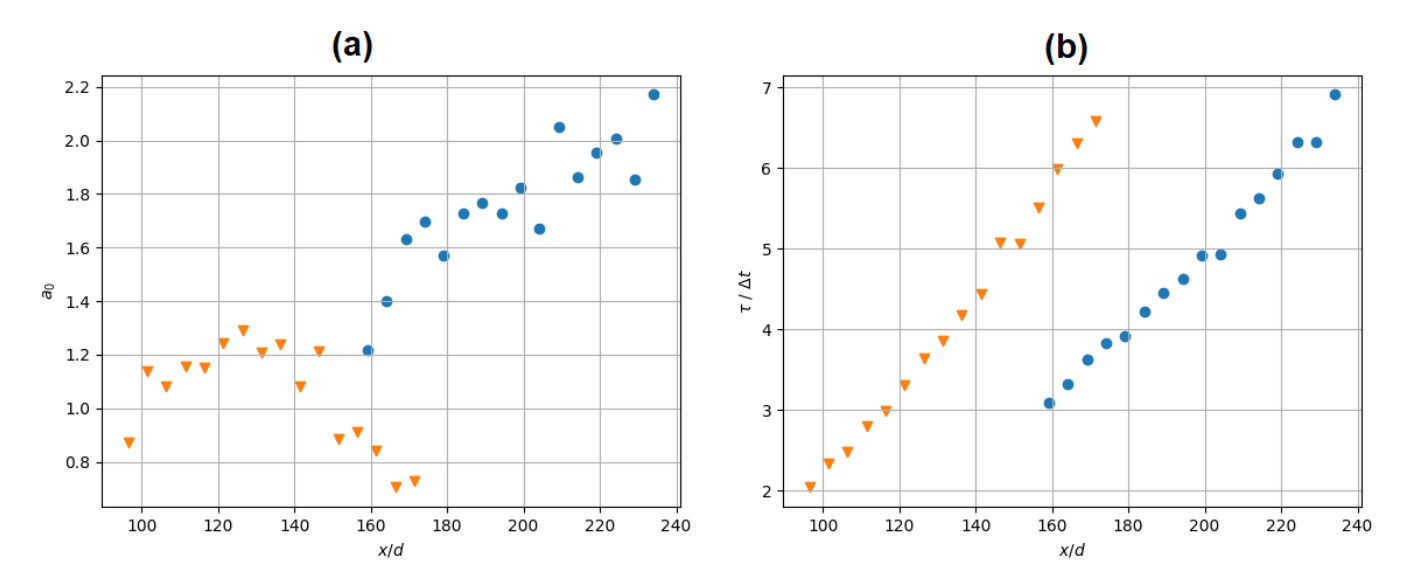


Figure 11: Assessment of Heisenberg Yaglom prediction. (a) Acceleration parameter a_0 and (b) time oversampling in respect to Kolmogorov timescale $\tau = \sqrt{\frac{v}{\epsilon}}$.

The found variation of a_0 with downstream distance was also suggested in a previous LPT study investigating the acceleration variance in a turbulent jet (Viggiano et al., 2021). They reported an increase of a_0 with downstream distance. However, this increase is partly due to finite particle effect, since for their tracer particles had a normalized diameter of $9 < d_p/\eta < 25$ in dependence of downstream position.

The authors observed that the scaling $a_0 \sim (d_p/\eta)^{-1.75}$ does not match the typically observed scaling, which has an exponent between -2/3 and -0.81. They suggested that this deviation may be due to anisotropy. The observed linear increase of a_0 considering data of the second FOV shown in Figure 11a is in line with this assumption, provided that finite size effects and anisotropy do not affect each other. This becomes clear considering that the observed linear increase of the Kolmogorov scale with downstream distance corresponds to a $a_0 \sim (d_p/\eta)^{-1}$ scaling, which together with the finite particle size effect leads to $a_0 \sim (d_p/\eta)^{-1.75}$ as observed by Viggiano et al. (2021). However, the data from the first FOV does not align with this explanation, which can be attributed to the challenges in accurately measuring acceleration statistics in LPT experiments. It is likely that a combination of multiple sources of error is responsible for the inconclusive results on the Heisenberg–Yaglom prediction. Firstly, dissipation on the centerline in the jet decreases

downstream, as does the Kolmogorov time scale $\tau = \sqrt{v/\varepsilon}$. This has significant implications for the statistics of the acceleration. It is known that due to the intermittency of acceleration, an oversampling in respect to the Kolmogorov timescale is necessary to capture rare high acceleration events in LPT experiments. Despite the oversampling of 2 to 7 times shown in Figure 11b, it can be assumed that tracks at particularly high accelerations could not be captured in some cases. This problem therefore occurs particularly close to the nozzle and can therefore lead to an underestimation of the acceleration variance, depending on the streamwise position. In light of the comparable patterns observed in Figure 11 with respect to the data of the second FOV, the disparate underestimation of acceleration variance indicates that this issue has a considerable impact on the estimation of a_0 .

Furthermore, STB results are filtered to reduce measurement noise. This is achieved by utilizing the TrackFit algorithm presented in (Gesemann et al., 2016), which is based on the definition of a cut-off frequency derived from the position spectrum of the tracks. This separates the actual position of the particles from the measurement error, which is modelled as white noise. This procedure corresponds to the application of an optimal Wiener filter, which contributes to a more accurate estimation of the variance by reducing the positional error.

The remaining error, which persists despite the filtering process, can be obtained from the initial positional error of 0.08mm for the streamwise direction in the first FOV and 0.06 mm for the second one, respectively. This error propagates also to the measurement of the variance of the acceleration (and also the velocity), leading to an additional acceleration variance. As the acceleration variance due to the positional error is additive, it must be subtracted for accurate results, as has been done for the presented statistics in Figure 11a and 6b. However, the cutoff frequency changes downstream due to the decreasing average velocities and accelerations. It would therefore be necessary to use locally different filters to properly separate the measurement error. This has not yet been implemented, so a global filter has been used which leads to an additional locationdependent error in the acceleration estimate. It should be noted that this type of error affects the first FOV data set in particular, which may contribute to the observed differences in the trends of a_0 between the two FOVs. This is due to the fact that the correct cut-off frequency changes more strongly here, as a result of the stronger change of flow conditions. A detailed description of the errors and the correction of the data will be the subject of future publications. The difficulties in obtaining accurate acceleration statistics are not limited to the experiments presented here, but extend to all LPT experiments. Consequently, it can be inferred that the results from earlier experiments by Viggiano et al. (2021), which had even less time oversampling, were also significantly influenced by the aforementioned effects. Thus, a comprehensive investigation of

measurement errors is necessary to conclude on the role of anisotropy to predict acceleration variance with the Heisenberg-Yaglom relation.

8. Conclusions and outlook

The (super-)far field of a round jet of air was investigated using Shake-The-Box Lagrangian-Particle-Tracking of Helium-Filled-Soap-Bubbles (HFSB). The measurement was conducted in a large test facility with a size of 6 $\,^4$ $\,^3$.4 $\,^3$ = 82 $\,^3$ containing a contraction nozzle of d = 10 mm diameter and an exit velocity of U_j = 49.75 m/s leading to a Reynolds number of Re_d = 33,000. A high effective seeding density of more than 0.1 particles per pixel was achieved using a two-volume scanning approach, allowing for the resolution of a wide range of scales in the flow.

The analysis of the dataset reveals self-similar scaling of streamwise velocity and variance in the investigated domain of 90 < x/d < 240.

The impact of the confinement on the backflow was evaluated through the examination of the relationship between the momentum of the jet and the momentum of the backflow. Despite the anticipated minimal influence of the confinement, a slight deviation in the velocity decay rate B was observed. This observation may be attributed to the potential influence of mean pressure differences, which could distort the jet and thus alter the statistical data collected. It is therefore postulated that the pressure differences induced by the spatial geometry, which should be particularly visible in our experiment due to the focus on the super far field, are responsible for the deviations. Despite these issues, the presented profiles of mean velocity and Reynold stresses expand the experimental confirmation of the similarity theory and the jet spreading rate to further downstream in the far field.

The investigation of instantaneous, iso-contour surfaces of velocity and Q-values demonstrate the stability of coherent structures and occasional backflow events at the TNT-interface of the jet to the still environment.

The shape of the coherent structures resembles tubes rather than hairpins, suggesting that almost no hairpin structures are generated in the far field.

Furthermore, a number of different methods based on structure functions were tested in order to ascertain their ability to predict the mean dissipation of turbulent kinetic energy. It was found that the velocity-acceleration structure function, which was analyzed considering particle separations in all three spatial directions, provided the best results in this regard. In contrast, the longitudinal and transverse velocity structure functions, which are typically used in this context, are rather inaccurate due to the anisotropy of the flow.

Furthermore, an estimation of the Heisenberg-Yaglom 'constant' using acceleration information obtained from the Lagrangian tracks and dissipation from the velocity-acceleration structure function is presented.

The results here are inconclusive, which we attribute to an inaccurate determination of the acceleration statistics due to the highly variable temporal oversampling which impedes tracking of particles with very high acceleration in some regions of the measurement area and requires a locally adjusted track filtering scheme which is not yet implemented.

A number of further areas for investigation can be derived from the problems described above. Firstly, new methods of data assimilation must be applied in order to obtain the velocity gradients and the pressure from the results with satisfactory accuracy despite the large inter-particle distance of the tracking result. To this end, extensions of FlowFit (Godbersen et al., 2024) and methods based on PINNs (Raissi et al., 2019) are being developed. Conversely, enhancements to the STB method are essential to permit the computation of accurate acceleration statistics even in this highly anisotropic flow. The current STB scheme is able to track such particles reliably, whose predicted position is reasonably close to the real position (the reprojected image has to overlap with the real particle image in at least a subset of cameras in order to allow a correction of the prediction). For highly accelerated particles, this might not be fulfilled, therefore an updated scheme to correct a predicted position is necessary. One such method as has been proposed as Variable-Space-Step-STB (Schanz et al., 2022). Other methods are feasible, e.g. a better prediction using either neighboring particles or an advected flowfield. Furthermore, a local filter must be developed to optimally filter out the measurement noise in flow regions with varying mean velocity and to determine the remaining error. The aforementioned improvements will permit an investigation into the extent to which the Heisenberg-Yaglom prediction is contingent upon anisotropies, as well as the investigation of other problems requiring accurate acceleration moments estimation in anisotropic flows.

Ackknowledgement

We thank Chris Willert and Michael Schroll from DLR, AT-OTM, Cologne for providing the round jet. We also express our gratitude to Abhijna Raghava Simhan and Hemanth Naidu Kotra for their contributions in setting up the experiment.

9. References

Alekseenko, S. V., Abdurakipov, S. S., Hrebtov, M. Y., Tokarev, M. P., Dulin, V. M., & Markovich, D. M. (2018). Coherent structures in the near-field of swirling turbulent jets: A tomographic PIV study. International Journal of Heat and Fluid Flow, 70, 363-379. https://doi.org/10.1016/j.ijheatfluidflow.2017.12.009

Ball, C. G., Fellouah, H., & Pollard, A. (2012). The flow field in turbulent round free jets. Progress in Aerospace Sciences, 50, 1-26. https://doi.org/10.1016/j.paerosci.2011.10.002

Batchelor, G.K. (1953) Pressure fluctuations in isotropic turbulence, Proc. Cambridge Philos. Soc. 47, 359 ~1950!.

Bevilaqua, P. M., & Lykoudis, P. (1978). Turbulence memory in self-preserving wakes. Journal of Fluid Mechanics, 89, 589–606.

Borgas, M. S. (1993). The multifractal Lagrangian nature of turbulence. Philosophical Transactions of the Royal Society of London. Series A: Physical and Engineering Sciences, 342(1665), 379-411.

Buaria, D., & Sreenivasan, K. R. (2022). Scaling of Acceleration Statistics in High Reynolds Number Turbulence. Phys. Rev. Lett., 128(23), 234502. https://doi.org/10.1103/PhysRevLett.128.234502

Capp, S. P. (1983). Experimental investigation of the turbulent axisymmetric jet. State University of New York at Buffalo.

Casey, T. A., Sakakibara, J., & Thoroddsen, S. T. (2013). Scanning tomographic particle image velocimetry applied to a turbulent jet. Physics of Fluids, 25(2), 025102. https://doi.org/10.1063/1.4790640

Clark, K. M., & Loth, E. (2013). A multi-scale LES technique for coupling near-field and far-field domains for a jet flow. Computers & Fluids, 88, 262-271. https://doi.org/10.1016/j.compfluid.2013.09.011.

Ganapathisubramani, B., Lakshminarasimhan, K., & Clemens, N. T. (2008). Investigation of three-dimensional structure of fine scales in a turbulent jet by using cinematographic stereoscopic particle image velocimetry. J. Fluid Mech., 598, 141–175.

George, W. K. (1989). The self-preservation of turbulent flows and its relation to initial conditions and coherent structures. Advances in Turbulence, 3973.

George, W. K. (2012). Asymptotic Effect of Initial and Upstream Conditions on Turbulence. ASME. J. Fluids Eng., 134(6), 061203. https://doi.org/10.1115/1.4006561

Gesemann, S., Huhn, F., Schanz, D., & Schröder, A. (2016). From Noisy Particle Tracks to Velocity, Acceleration and Pressure Fields using B-splines and Penalties. 18th Lisbon Symposium, Portugal

Godbersen, P., Gesemann, S., Schanz, D., & Schröder, A. (2024). FlowFit3: Efficient data assimilation of LPT measurements. 21th Lisbon Symposium, July 8 -11. Lisbon, Portugal.

Hussein, H. J., Capp, S. P., & George, W. K. (1994). Velocity measurements in a high-Reynolds-number, momentum-conserving, axisymmetric, turbulent jet. Journal of Fluid Mechanics, 258, 31–75.

https://doi.org/10.1017/S002211209400323X

Kuhn, P., Oberleitner, K., & Soria, J. (2018). Identification of coherent structures in the far field of a turbulent jet based on spectral proper orthogonal decomposition of time-resolved PIV snapshots. 19th Lisbon Symposium, Portugal.

Kwon, S. J., & Seo, I. W. (2005). Reynolds number effects on the behavior of a non-buoyant round jet. Experiments in Fluids, 38, 801-812.

La Porta, A., Voth, G., Crawford, A.M., Alexander, J., Bodenschatz, E. (2001). Fluid particle accelerations in fully developed turbulence. Nature, 409, 1017–1019. https://doi.org/10.1038/35059027

Lawson, J. M., Bodenschatz, E., Lalescu, C. C., & Wilczek, M. (2018) Bias in particle tracking acceleration measurement. Exp Fluids, 59, 172. https://doi.org/10.1007/s00348-018-2622-0

Mann, J., Ott, S., & Andersen, J. S. (1999). Experimental study of relative, turbulent diffusion. Tech. Rep. Risø–R–1036(EN). Risø National Laboratory.

Matsuda, T., & Sakakibara, J. (2005). On the vortical structure in a round jet. Physics of Fluids, 17(2), 025106. https://doi.org/10.1063/1.1840869

Monin, A.S, & Yaglom, A.M. (1975) Statistical Fluid Mechanics: Mechanics of Turbulence, vol. 2. MIT Press

Panchapakesan, N. R., & Lumley, J. L. (1993). Turbulence measurements in axisymmetric jets of air and helium. Part 1. Air jet. Journal of Fluid Mechanics, 246, 197–223. doi:10.1017/S0022112093000096

Qureshi, N. M., Bourgoin, M., Baudet, C., Cartellier, A., & Gagne, Y. (2007). Turbulent transport of material particles: an experimental study of finite size effects. Phys. Rev. Lett., 99(18), 184502.

Raissi, M., Perdikaris, P., & Karniadakis, G. E. (2019). Physics-informed neural networks: A deep learning framework for solving forward and inverse problems involving nonlinear partial differential equations. Journal of Computational Physics, 378, 686-707. https://doi.org/10.1016/j.jcp.2018.10.045

Romano, G. P., & Antonia, R. A. (2001). Longitudinal and transverse structure functions in a turbulent round jet: effect of initial conditions and Reynolds number. J. Fluid Mech., 436, 231–248.

Sawford, B. L., Yeung, P. K., Borgas, M. S., Vedula, P., La Porta, A., Crawford, A. M., & Bodenschatz, E. (2003). Conditional and unconditional acceleration statistics in turbulence. Physics of Fluids, 15(11), 3478–3489. https://doi.org/10.1063/1.1613647

Schanz, D., Gesemann, S., & Schröder, A. (2016). Shake The Box: Lagrangian particle tracking at high particle image densities. Exp. Fluids, 57(70).

Schanz, D., Jahn, T., & Schröder, A. (2022). 3D particle position determination and correction at high particle densities. In Proceedings of the 20th International Symposium on the Application of Laser and Imaging Techniques to Fluid Mechanics (pp. 1933-1949). Lisbon, Portugal. ISBN 978-989-53637-0-4.

Schanz, D., Novara, M., & Schröder, A. (2021). Shake-The-Box particle tracking with variable time-steps in flows with high velocity range (VT-STB). In Proceedings of 14th International Symposium on Particle Image Velocimetry (Vol. 1, No. 1, pp. 1-11). ILLINOIS Tech/Paul V. Galvin Library.

Schanz, D., Schröder, A., Bosbach, J., Strübing, T., Wolf, C., Schwarz, C., & Heintz, A. (2024). Scanning Lagrangian Particle Tracking to measure 3D large scale aerodynamics of quadcopter flight. In 21st International Symposium on Applications of Laser and Imaging Techniques to Fluid Mechanics, 08 - 11 July 2024, Lisbon, Portugal.

Schröder, A., Schanz, D., Gesemann, S., Huhn, F., Buchwald, T., Garaboa-Paz, D., & Bodenschatz, E. (2022). Measurements of the energy dissipation rate in homogeneous turbulence using dense 3D Lagrangian Particle Tracking and FlowFit. In Proceedings of the 20th International Symposium on the Application of Laser and Imaging Techniques to Fluid Mechanics (No. 216, pp. 2300-2319).

Schröder, A., & Schanz, D. (2023). 3D Lagrangian Particle Tracking in Fluid Mechanics. Annual Review of Fluid Mechanics, 55(1), 511–540.

Staack, K., Reinhard, G., Schröder, A. (2010) 3D3C-coherent structure measurements in a free turbulent jet. 15th International Symposium on Application Laser Techniques to Fluid Mechanics, 2010-07-05 - 2010-07-08, Lisbon, Portugal.

Sciacchitano, A., Leclaire, B., & Schroeder, A. (2021). Main results of the first data assimilation challenge. In Proceedings of 14th International Symposium on Particle Image Velocimetry (Vol. 1, No. 1, pp. 1-13). ILLINOIS Tech/Paul V. Galvin Library.

Sreenivasan, K. R., & Narasimha, R. (1982). Equilibrium Parameters for Two-Dimensional Turbulent Wakes. Trans. ASME J. Fluids Eng., 104, 167–169.

Tso, J., & Hussain, F. (1989). Organized motions in a fully developed turbulent axisymmetric jet. Journal of Fluid Mechanics, 203, 425-448. doi:10.1017/S0022112089001539

Viggiano, B., Basset, T., Solovitz, S., Barois, T., Gibert, M., Mordant, N., ... Cal, R. B. (2021). Lagrangian diffusion properties of a free shear turbulent jet. Journal of Fluid Mechanics, 918, A25. doi:10.1017/jfm.2021.325

Volk, R., Calzavarini, E., Lévêque, E., & Pinton, J.-F. (2011). Dynamics of inertial particles in a turbulent von Kármán flow. J. Fluid Mech., 668, 223–235.

Voth, G. A., La Porta, A., Crawford, A. M., Alexander, J., & Bodenschatz, E. (2002). Measurement of particle accelerations in fully developed turbulence. Journal of Fluid Mechanics, 469, 121–160. doi:10.1017/S0022112002001842

Wygnanski, I., & Fiedler, H. (1969). Some measurements in the self-preserving jet. Journal of Fluid Mechanics, 38(3), 577–612. doi:10.1017/S0022112069000358

Yeung, P.K., Pope, S.B., Lamorgese, AG., Donzis, D.A. (2006) Acceleration and dissipation statistics of numerically simulated isotropic turbulence. Physics of Fluids; 18 (6): 065103. https://doi.org/10.1063/1.2204053

Yeung, P. K., Zhai, X. M., & Sreenivasan, K. R. (2015). Extreme events in computational turbulence. Proceedings of the National Academy of Sciences, 112(41), 12633-12638.

Yoda, M., Hesselink, L., Mungal, M.G. (1992) The evolution and nature of large-scale structures in the turbulent jet. Phys. Fluids; 4 (4): 803–811. https://doi.org/10.1063/1.858297

Zhou, K., Grauer, S. J., Schanz, D., Godbersen, P., Schröder, A., Rockstroh, T., Jeon, Y. J., & Wieneke, B. (2024).

Benchmarking data assimilation algorithms for 3D Lagrangian particle tracking. In 21th Lisbon Symposium, July 8 - 11. Lisbon, Portugal.